Annals of Nuclear Energy 113 (2018) 147–161

Contents lists available at ScienceDirect

Annals of Nuclear Energy

journal homepage: www.elsevier.com/locate/anucene

Neutronic analysis for accident tolerant cladding candidates in CANDU-6 reactors

A. Naceur *, G. Marleau

Institut de Génie Nucléaire, École Polytechnique de Montréal, P.O. Box 6079, Station Centre-Ville, Montréal, Québec H3C 3A7, Canada

ARTICLE INFO

Article history:
Received 14 July 2017
Received in revised form 6 November 2017
Accepted 8 November 2017
Available online 20 November 2017

Keywords:
CANDU-6
Accident tolerant claddings
Zicaloy-II
SiC
FeCrAl
APMT
304SS
310SS

ABSTRACT

The neutronic penalty and advantages are quantified for potential accident tolerant claddings in a CANDU-6 (Canada Deuterium Uranium) reactor. Ferritic-based alloy (FeCrAl and APMT), steel-based alloy (304SS and 310SS) and silicon carbide (SiC) claddings are compared with Zircaloy-II. High thermal capture in nickel-59 and iron-56 imply a neutronic penalty in iron and steel-based bundles. A minimum enrichment of 1.0% and 1.1% is required for ferritic and steel-based claddings, respectively, to achieve the CANDU-6 burnup average criticality. An average increase of 0.35% in reactivity is introduced when SiC is considered, while keeping a natural enrichment condition. Average thermal neutron absorption rate is found to be 203, 8 and 6 times higher in UO_2 pellets than in silica, iron and steel-based claddings, respectively. A spectral hardening is observed in fuel, cladding and coolant for all enriched cells. Neutron flux is 30.5% higher at 0.0253 eV in SiC and Zr bundles. For FeCrAl, APMT, 304SS and 310SS, less ^{239}Pu is produced during all fuel residence time and a minimum of 50% more ^{135}Xe poison is being produced at equilibrium. As well, a minimum of 60% more ^{235}U is left at end-of-life. For bundles cladded with SiC and Zr, 7.6% higher fission rates are found on the pellet periphery. Decreasing the cladding thickness by 200 μm made it possible to satisfy the criticality requirements for all claddings with an enrichment below 1%. Moderator and coolant temperature coefficients are found higher in SiC and Zr bundles. At mid-burnup, the Doppler effect and the voiding effect are higher in FeCrAl, APMT, 304SS and 310SS cladded cells.

1. Introduction

Following the station blackout (SBO) accident at three units of the Japanese Fukushima Daiichi Nuclear Power Station, caused by the 2011 Tohoku earthquake and tsunami, fuel system improvement has become a subject of intense concern (Burns et al., 2012). The new strategy is to develop a fuel pin that can tolerate severe accident scenarios. Accident Tolerant Fuels (ATF) have to provide significant improvements in safety response, resulting from a loss in cooling capacity, while maintaining a good operational neutronic performance during normal conditions. Substantially improved safety responses have to cover the entire spectrum of design basis (DB) and beyond design basis (BDB) accidents (Ott et al., 2014). The accident tolerant fuel system should suppress or reduce the steam-cladding oxidation rate, minimize the additional heat generation, enhance hydrogen sequestration when generated, improve fuel and cladding retention of fission products and maintain core coolability (Zinkle et al., 2014). The new system should exhibit a good structural integrity at the UO_2/Zr rod burst point expected in the temperature range [700—1200]°C. By delaying the cladding ballooning and burst point and reducing its specific mass change at 1200°C in steam condition, ATF concepts aim to delay hydrogen accumulation from proceeding (Zinkle et al., 2014).

The first and the easiest approach to develop ATF is to introduce some modifications in existing Zircaloy alloy in order to improve the material dimensional performance and oxidation kinetics. Sixty years of Zr alloy development suggest that such investigations are not able to produce significant differences in BDB response (Zinkle et al., 2014). The major problems affecting loss of coolant accident (LOCA), reactivity initiated accident (RIA) and SBO are the Zr hydride formation at high burnups and the Zr heat production by oxidation above 1200°C, that will surpass radioactive decay and increase substantially the heat removal requirement (Terrani et al., 2014). The second approach is to consider a markedly different non-zirconium cladding with high performance in oxidation resistance. The third approach is to develop an alternative fuel form to the current ceramic oxide uranium pellet with one or more additional barriers to fission products retention (Terrani et al., 2012). This paper focuses on the second approach

* Corresponding author.
E-mail addresses: ahmed.naceur@polymtl.ca (A. Naceur), guy.marleau@polymtl.ca (G. Marleau).

https://doi.org/10.1016/j.anucene.2017.11.016
0306-4549/

by choosing among ATF cladding concepts specific iron-based alloys (FeCrAl and APMT), steel-based alloys (304SS and 310SS) and silica (SiC) options. This work pursues George et al. (2015) analysis on PWR for a CANDU-6 reactor.

A number of experimental investingations were performed by Pint et al. (2013) at 800–1500°C in 1–20 bar steam condition and H_2-H_2O environments and they all emphasized the performance of these claddings. The basic FeCrAl alloy appears a promising oxidation resistant material by forming a protective aluminium-rich oxide at 800°C, 1000°C (at 10.3 bar) and 1200°C. The protective alumina scale was resistant up to 1475°C. Y and Hf additions in Kanthal alloy APMT (Advanced Powder Metallurgy Tube) shows an excellent alumina scale adhesion (a solid diffusion barrier) after 48 h at 1200°C and 8 h at 1350°C. Conventional 304-type stainless steel cladding is more resistant in steam condition than the current Zircaloy to ballooning and burst points but not at 1200°C. Also because of the scale spallation, a significant mass change is observed at 1000°C. The study of this sheath will be maintained for its high burnup capability (Uwaba et al., 2011) and irradiation performance in PWRs before 1960 (George et al., 2015). The 304SS poor relative oxidation performance can be mitigated by increasing its chromium and/or nickel contents (as in 310SS). Austenitic type 310 stainless steel forms a thin chromia, showing a good protective behavior at 1200°C in steam condition. Silicone carbide (SiC) demonstrates exceptional oxidation resistance and an excellent integrity in high-pressure and temperature steam–H_2 environments. SiC-based bundle is difficult to fabricate, shows the formation of volatile hydroxides and low thermal conductivity when irradiated.

The present work compares the neutronic performance of these candidates with the baseline zirconium alloy (Zr-II) bundle, using burnup calculations, isotope depletion analyses, absorption rate ratios, spectral and spatial self-shielding analysis, plutonium radial profile and reactivity perturbations. It also allows us to answer the question whether enrichment is necessary for an implementation in CANDU-6 reactors and if these enrichment levels could be avoided by a pin geometry optimization. In Section 2, we present the CANDU-6 lattice modeling, the candidate cladding parameters and the enrichment methodology. In Section 3, we analyze the cell behavior under normal, optimized and accidental conditions. In Section 4, we conclude and highlight future work.

2. Methodology

2.1. CANDU-6 lattice modeling and parameters

A typical CANDU-6 cell geometry consists of a fuel bundle surrounded by two concentric pressure and calandria tubes, where the gap between the inner and the outer cylinder is filled with helium gas. This gas is inserted to ensure insulation between the hot D_2O coolant and the cold moderator. The calandria tube is surrounded by a D_2O moderator. For the purpose of this study, a standard fuel bundle was used and is illustrated in Fig. 1. It consists of 37 fuel pins arranged in an annular ring formation (1, 6, 12 and 18) for a lattice pitch of 28.575 cm. Every fuel pin consists of 30 natural uranium oxide (UO_2) pellets that are stacked inside a zirconium alloy cladding tube. A similar type of alloy is used for the calandria tube and a Zr-Nb alloy for the pressure tube.

The heavy water moderator purity is assumed to be 99.92 at.%. The coolant purity is 99.3 at.%. The data relative to the reference cell model are listed in Table 1, with IR and OR being the inner and the outer radii, respectively. All fuel elements have the same radii, the same isotopic compositions, the same density and temperature. We introduced four identical mixtures for each rod to take into account different burnup levels that might occur

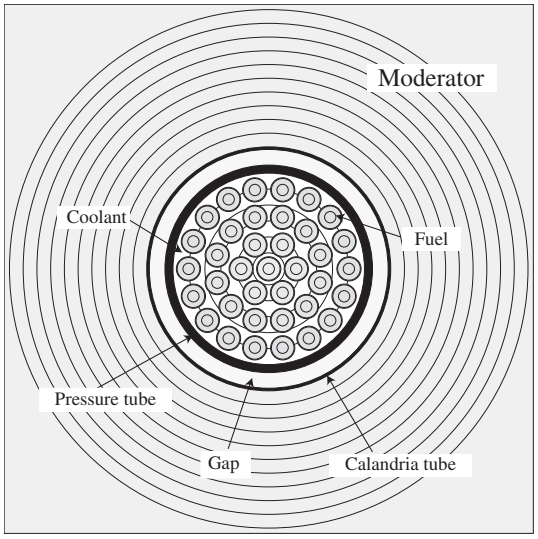

Fig. 1. Standard 37-element bundle cell.

Table 1
CANDU-6 cell parameters for [UO_2-Zr] fuel.

Structure	Material	Density [g/cm^3]	T [K]	IR [cm]	OR [cm]
Coolant	D_2O	0.8121	560.66	0.0000	5.1689
Pressure Tube	Zr-Nb	6.5700	560.66	5.1689	5.6032
Helium Gap	$^4_2$He	0.0014	345.66	5.6032	6.4478
Calandria Tube	Zr-II	6.4400	345.66	6.4478	6.5875
Moderator	D_2O	1.0829	345.66	6.5875	14.288
Fuel	UO_2	10.438	941.29	0.0000	0.6122
Cladding	Zr-II	6.4400	560.66	0.6122	0.6540

Table 2
CANDU-6 cluster geometry properties.

Ring (i)	n_i	r_i [cm]	θ_i [rad]
1	1	0.0000	0.0000
2	6	1.4885	0.0000
3	12	2.8755	0.261799
4	18	4.3305	0.0000

depending on how far the pins are from the moderator. The pellet-cladding gap and fuel element dimensions will be adjusted only in the case of cycle reactivity improvement. The four fuel cluster rings, denoted Ring (i) in Table 2, contain respectively n_i pins located on a circle of a radius r_i with θ_i the angular position of the first pin. The other pins are distributed uniformly on the circle.

2.2. Claddings parameters

Table 3 lists the cladding materials used for fuel reactivity calculations, densities (in g/cm^3) and detailed isotopic compositions (in weight percentage). In our study, the baseline zirconium alloy (Zircaloy-II) is compared with five different candidates: silicon carbide (SiC), ferritic iron chromium aluminum alloy (FeCrAl), 304 stainless steel (304SS), austenitic type 310 (310SS) and kanthal advanced powder metallurgical (APMT). These claddings were considered because of their sufficient oxidation resistance at a significantly higher melting point than for Zircaloy. For conventional stainless steel (304SS), increasing the Cr and Ni contents (as 25Cr-20Ni in 310SS) provides a good steam oxidation resistance

Table 3
Isotopic compositions (wt.%) of candidate claddings materials.

Material	ρ_v [g/cm^3]	^{56}Fe	^{58}Ni	^{52}Cr	^{nat}B	^{91}Zr	^{28}Si	^{12}C	^{27}Al	^{59}Ni	^{55}Mn	^{96}Mo	^{179}Hf
Zircaloy-II	6.44	0.16	0.06	0.11	0.00031	99.71	–	–	–	–	–	–	–
SiC	2.58	–	–	–	–	–	70.08	29.92	–	–	–	–	–
FeCrAl	7.10	75.0	–	20.0	–	–	–	–	5.0	–	–	–	–
304SS	7.90	71.35	–	18.9	–	–	0.42	–	–	8.35	0.70	0.27	–
310SS	8.03	52.55	–	25.22	–	–	0.7	–	–	19.51	1.9	0.122	–
APMT	7.30	69.79	–	21.60	–	0.10	0.53	–	4.9	–	–	2.92	0.16

at 1200°C (Pint et al., 2013). Fig. 2 compares the macroscopic capture cross sections (Σ_c) of cladding materials. As one can see, in the thermal region ($E < 0.625$ eV), we distinguish two different classes of response. The first class of response correspond to that of Zr and SiC. FeCrAl, APMT, 304SS and 310SS form the second class of response. The latter is characterized by a high neutron capture cross section compared with Zr and SiC responses. This trend is mainly due to the fact that these materials contain at least 52% iron, a material that has an absorption cross section in the thermal groups of the order of 10 barns. Stainless steel claddings have a larger thermal neutron absorption due to the captures of nickel-59. 310SS has more thermal neutrons captures because the nickel-59 content is 11% higher than in 304SS. The two APMT peaks that are seen in the epithermal zone are due to the presence of ^{96}Mo. However, as expected, nuclei having magic numbers of neutrons ($^{9}_{40}$Zr) or a doubly semi-magic number ($^{28}_{14}$Si) show low tendency in capturing neutrons (Glasstone and Sesonske, 2012; Cottingham and Greenwood, 2002). For thermal, epithermal and fast neutrons, SiC cladding is more transparent than the baseline zirconium alloy. In normal conditions, the neutrons are slowed down in the moderator and then penetrate the neighboring bundles. Before initiating the next fission, they must succeed in crossing the sheath thickness. Thus, despite their better oxidation resistance, claddings with higher capture properties have a pronounced impact on the neutron balance.

2.3. Enrichment and geometry requirements

The five cladding materials react differently in the thermal and epithermal zones. An enrichment in ^{235}U will be required to compensate the different neutronic losses. The criteria suggested to determine the adequate enrichment for a cladding is that the fuel must have at least the fuel residence time Δt_c of the reference CANDU bundle. For each enriched cell, the effective neutron multiplication factor ($\bar{k}_{\text{eff}}$) d over the complete cycle must be equal to the effective reference [UO_2, Zr] criticality ($\bar{k}_{\text{eff,Zr}}$) without poison (St-Aubin and Marleau, 2015).

$$\bar{k}_{\text{eff}} = \frac{1}{\Delta t_c}\int_0^{\Delta t_c} k_{\text{eff}}(t)\, dt = \bar{k}_{\text{eff,Zr}}. \tag{1}$$

The fuel residence time is the reactor calendar time between the insertion of a single batch of fuel in the core and its extraction (Rouben, 2003). One alternative to using such a simple time averaged multiplication factor is to consider the following method. One first evaluates the time averaged cell homogenized two group cross sections and use them to calculate the k_{eff} solution to the equivalent homogeneous transport problem. This method is more coherent with how full reactor calculations are performed. However the two multiplication constants only differ by about 0.3 mk and leads to a maximum change in initial fuel enrichment of 0.001% which can be neglected for this study. For the CANDU-6 reactor, the fuel

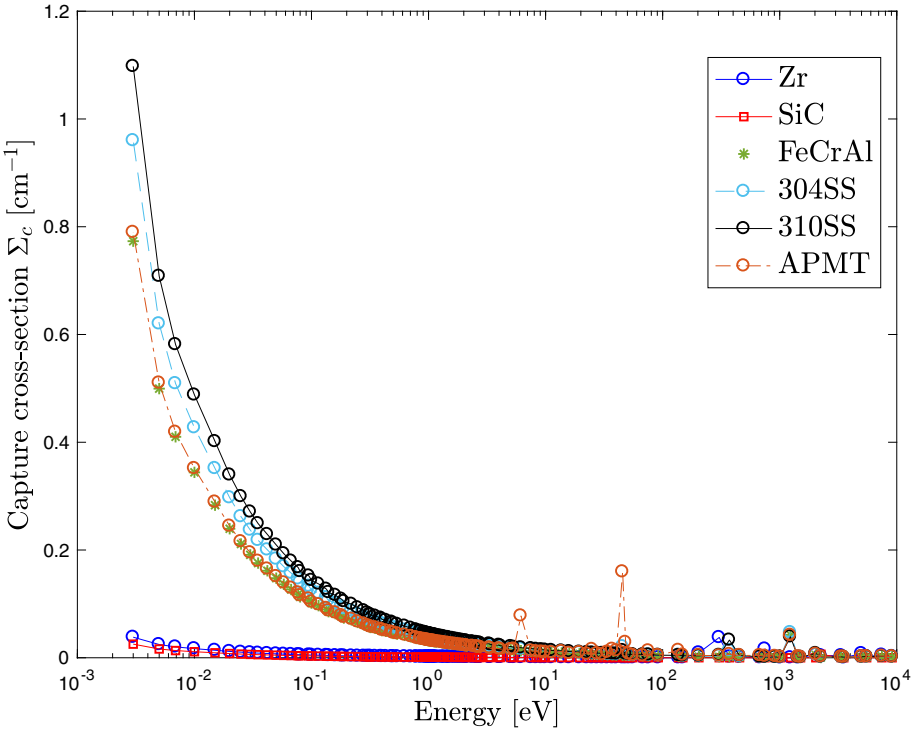

Fig. 2. Macroscopic capture cross section.

Table 4
Various fuel pin configurations used for reactivity improvement.

Case	e_{UO_2}	Pellet OR [cm]	Gap thickness [μm]	Clad OR [cm]	ϵ [μm]
$\mathcal{C}_0$ (Ref.)	e_{enr_U}	0.61220	0.0000	0.65400	418
$\mathcal{C}_1$	e_{enr_U}	0.61220	0.0000	0.63400	218
$\mathcal{C}_2$	e_{enr_U}	0.63220	0.0000	0.65400	218
$\mathcal{C}_3$	e_{enr_U}	0.61220	200.00	0.65400	218
$\mathcal{C}_4$	e_{nat_U}	0.61220	0.0000	0.63400	218
$\mathcal{C}_5$	e_{nat_U}	0.63220	0.0000	0.65400	218
$\mathcal{C}_6$	e_{nat_U}	0.61220	200.00	0.65400	218

residence time is the same as the cycle operation length and 300 days is considered for a complete burnup cycle at a constant power of 31.9713 kW/kg (exit burnup of 9.6 GW-day/tonne).

For natural and optimized enrichment, three fuel rod configurations are also considered. In the first one, the pellet dimension is kept constant and the cladding thickness ϵ is reduced by decreasing the external radius ($\mathcal{C}_1$ and $\mathcal{C}_4$). In the second, ϵ is reduced by increasing the pellet external radius ($\mathcal{C}_2$ and $\mathcal{C}_5$). In the third arrangement, the cladding thickness is reduced by increasing the void gap and keeping the pellet dimensions fixed ($\mathcal{C}_3$ and $\mathcal{C}_6$). In all cases, ϵ is reduced by 200 μm. Table 4 provides the various geometries studied for reactivity improvement. The fuel density is kept at 10.4375 g/cm^3 and the cladding densities for the different configurations are provided in Table 3. Analyses are performed for all cladding materials for Cases $\mathcal{C}_0$ to $\mathcal{C}_6$. Here, e_{UO_2} represents the uranium enrichment with $e_{nat_U} = 0.71140$ wt.% for natural uranium and e_{enr_U} the optimized fuel enrichment. $\mathcal{C}_0$ (Ref.) represents the actual CANDU-6 fuel pin geometry with optimized enrichment (e_{enr_U}), if needed.

2.4. Simulation strategy

Computation of the bare cell lattice properties constitutes the first stage of CANDU reactor physics simulations. The cell includes fuel elements, coolant, pressure tube, helium gap, calandria tube and moderator, but excludes all interstitial reactivity devices (Varin et al., 2004). Here, our analysis is based on the 3D lattice transport-theory code DRAGON5 (Marleau et al., 2016), which is part of the Industry Standard Tool-set (IST) of Codes for CANDU reactor core design and analysis (Rouben, 2002). The transport calculation in DRAGON were performed using the collision probability (CP) technique (Marleau et al., 1992).

Neutron cross sections are first extracted from a multigroup library. In this study, we used a 172-group WIMSD4 format library, based on JEFF 3.1 evaluated nuclear data (Koning et al., 2006). The two-dimensional Cartesian cell of Fig. 1 with reflective boundary conditions is considered. Normal CANDU-6 operation conditions (i.e. pressures, temperatures and densities) are assumed for all cells. For every zone, the CP integration lines are generated using the NXT tracking module (Marleau, 2005). At every burnup step, the cross sections are corrected by the generalized Stamm'ler resonance self-shielding approach (Hébert and Marleau, 1991). Tracking lengths are recovered by the ASM algorithm and the collision probability matrix is produced. The transport equation is finally solved without leakage. Then, the converged multi-group flux map is obtained. Two groups burnup dependent ($\mathcal{B}$) reaction rates, diffusion coefficients $D^g(\mathcal{B})$, condensed and homogenized macroscopic cross sections $\Sigma_x^g(\mathcal{B})$ are then produced for cell analysis and subsequent core calculations. During burnup calculation, the energy released outside the fuel is neglected. Yet, the clad composition variation due to neutron activation is taken into account. Our simulation strategy was verified with SERPENT Monte-Carlo code (Leppänen, 2013) using 10,000 neutrons per cycle, 2000 active batches and 200 inactive batches. As one can see in Table 5, the agreement between DRAGON and SERPENT is very good with differences in $k_{eff}(t_0)$ that remain below 2 mk.

3. Results

3.1. Depletion k_{eff} results

For natural enrichment (e_{nat_U}), Fig. 3 shows the evolution of the effective multiplication factor during one operation cycle. The two types of behavior previously observed for Σ_c responses (Fig. 2) are also noticed in the k_{eff} pattern. The same order of responses from the most to the least transparent material to thermal neutrons is reproduced. At begin of cycle (BOC), $t_0 = 0$ days, the bundle contains only fresh fuel. As the fuel depletes ($t > t_0$), different changes occur in fuel isotopic compositions depending on the cladding absorption cross section. Neutron radiative capture in ^{238}U lead immediately to the production of ^{239}U which, after a β^- decay (24 min), produces neptunium. The ^{239}Pu production is not immediate. There is a delay associated with ^{239}Np decay, which has a half-life of about 56 h (Burns et al., 2012). Hence, the rise observed on the 5th day is caused by the ^{239}Pu positive contribution. For e_{nat_U} condition, all cells display a ^{239}Pu peak, but for FeCrAl, APMT, 304SS and 310SS cladded fuels, the cell is initially and remains subcritical. We conclude that a chain reaction cannot be sustained and an increased enrichment is necessary.

To increase the cell reactivity, several iterations were needed to select the adequate enrichment. A convergence criterion of 10^{-2} pcm is selected. Fig. 4 depicts the dependence of k_{eff} on time, assuming the fuel enrichment is selected in such a way that Eq. 1 is satisfied for each cladding material. Fig. 5 shows the difference in the k_{eff} between the alternate cladding material and Zircaloy. Table 5 presents the converged results when the criticality criteria is satisfied for all cells. A higher neutron absorption probability implies a higher enrichment. At BOC, ^{235}U is the only fissile nuclei present in the fuel. For this reason, as the cell is more enriched, the initial supercriticality is found greater at this moment. At each time step, ^{235}U isotope proportions in enriched bundles is larger than for natural uranium fueled cells. Thermal absorption probability in this fissile isotope is 100 times larger than capture probabilities in ^{238}U. In other words, at each burnup step, ^{235}U fission is more plausible than ^{239}Pu production. This conclusion can be

Table 5
Cycle converged mean multiplication factor.

	Zr	SiC	FeCrAl	304SS	310SS	APMT
$k_{eff}(t_0, e_{nat_U})$	1.118047	1.122149	0.975665	0.944769	0.923572	0.971555
$\bar{k}_{eff}(e_{nat_U})$	1.026239	1.029790	0.922744	0.899505	0.884282	0.919418
e_{UO_2} [%]	0.711400	0.711400	1.049840	1.132900	1.192371	1.061905
$\bar{k}_{eff}(e_{UO_2})$	1.026239	1.029790	1.026239	1.026239	1.026239	1.026239
$\Delta k_{eff}(t_0)$ [DRAGON-SERPENT] [pcm]	50.7	167.9	54.1	81.9	34.2	90.0

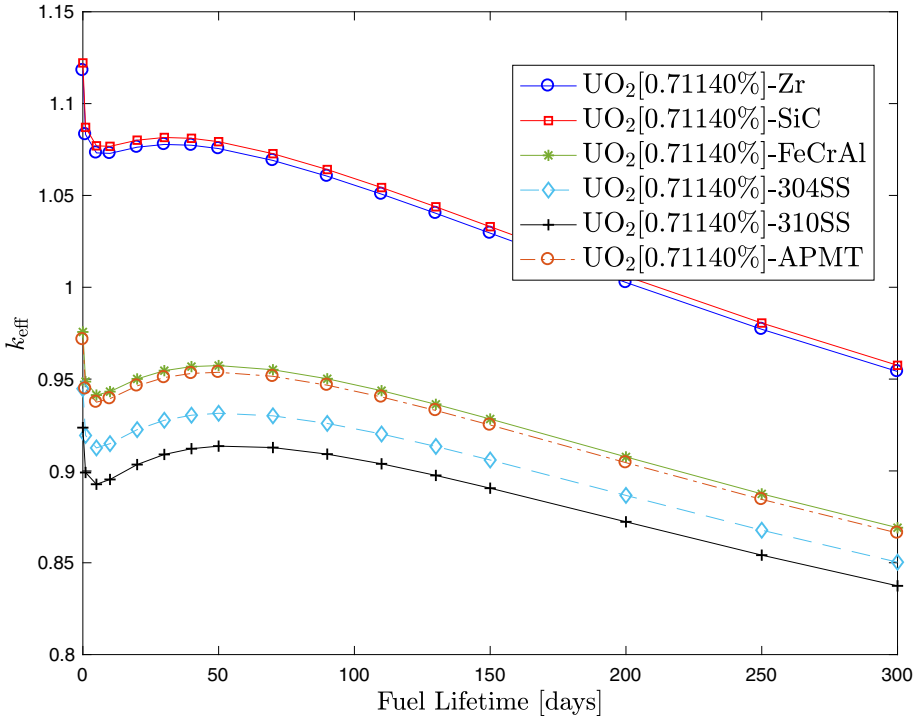

Fig. 3. Effective multiplication factor vs. fuel residence time in a standard CANDU-6 natural cell lattice.

confirmed by plutonium and uranium isotopes inventory evolution shown in Fig. 6. Consequently, the ^{239}Pu peak disappears for enriched fuels (see Fig. 4) and k_{eff} decreases more quickly. The supercriticality of the ferritic sheath cells surpasses the silicon cell up to the 70th day and continues to dominate the reference cell criticality until the 110th day. Then, the multiplication constant for ferretic cladded cells becomes lower than that observed for cells cladded with Zr and SiC (natural uranium fuel). This behavior can be more easily seen in Fig. 5. After these burnup periods, the ^{235}U fission rate is no longer able to compensate the neutronic penalty. The more transparent SiC cladding produces a positive 0.35% $\Delta\bar{k}_{\text{eff}}$ during all fuel residence period. A higher boron concentration will be

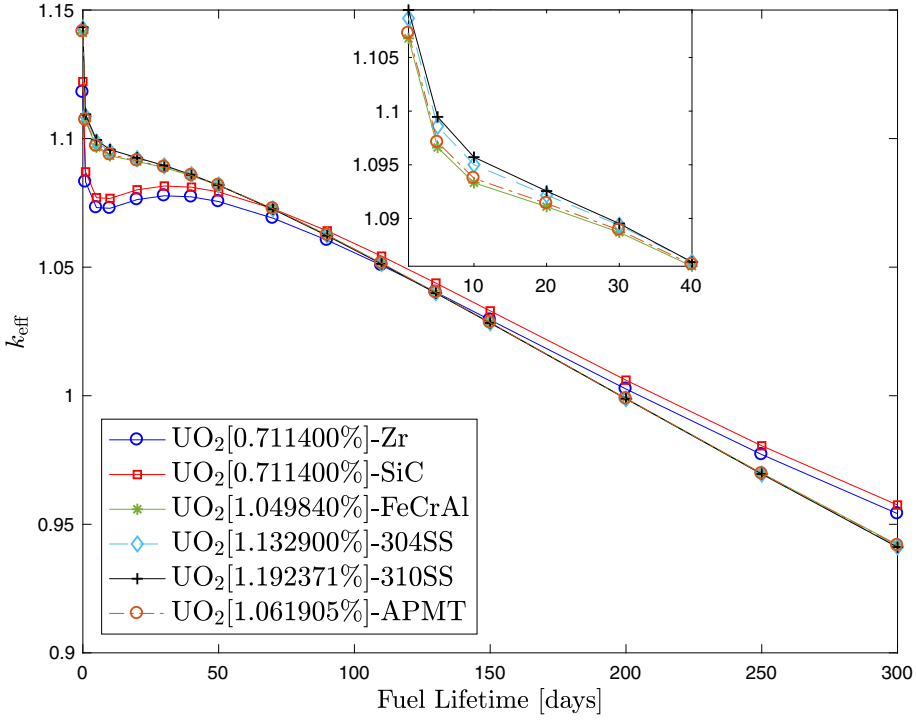

Fig. 4. Effective multiplication factor vs. fuel residence time for various cladding candidates in a standard CANDU-6 cell lattice.

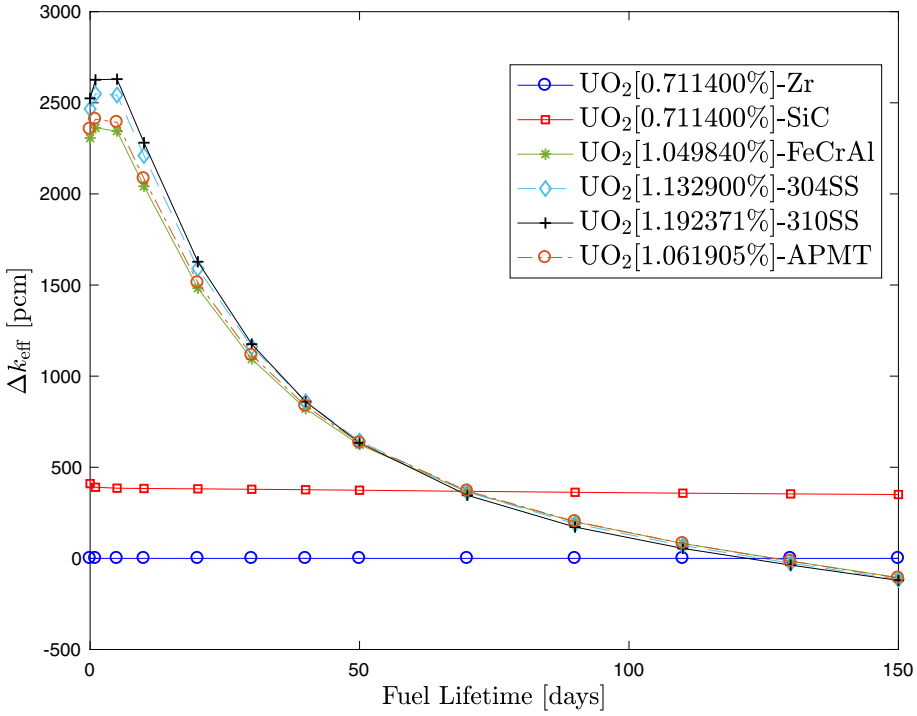

Fig. 5. Δk_{eff} from Zircaloy-II vs. fuel residence time for various cladding candidates in a standard CANDU-6 cell lattice.

needed for SiC bundle criticality control. Fig. 7 depicts xenon and ruthenium accumulation as a function of the fuel residence time. As one can see, the concentration of xenon decreases regularly after having reached a maximum (time between 50 and 100 days, depending on the fuel enrichment). This is expected even for high-flux reactor where the xenon concentration is proportional to

$$\frac{\sum_j N_j(t)\sigma_{j,f}}{\sigma_{Xe,a}}$$

(one group microscopic cross sections assumed constant), with N_j and $\sigma_{j,f}$, respectively, the concentration and the fission microscopic cross section of the fissile isotope j. $\sigma_{Xe,a}$ is the ^{135}Xe absorption microscopic cross section. Thus changes in the fissile isotopes concentration will affect the xenon production rate and its concentration in the fuel. Initially, the loss of ^{235}U is completely compensated by ^{239}Pu creation with its larger thermal fission cross section. As the fuel reaches higher burnups, the concentration of xenon decreases because the global concentration of fissile isotopes leads to a smaller macroscopic fission cross section. Table 6 lists the time average fuel absorption rate over cladding absorption rate for slow, epithermal and fast neutrons. These results emphasize the cladding role seen in k_{eff} depletion results. While the slow neutron absorption rate is 203 times more pronounced in UO_2 pellets than in SiC cladding, this ratio is reduced to 136, 8.1, 8.0, 6.8 and 6.2, respectively, for Zr, FeCrAl, APMT, 304SS and 310SS claddings.

3.2. Neutron spectrum

At each burnup step, cross sections were homogenized over fuel, cladding and moderator mixtures. The normalized flux (ϕ_m^g) per unit fission was produced at each of the 172 energy groups

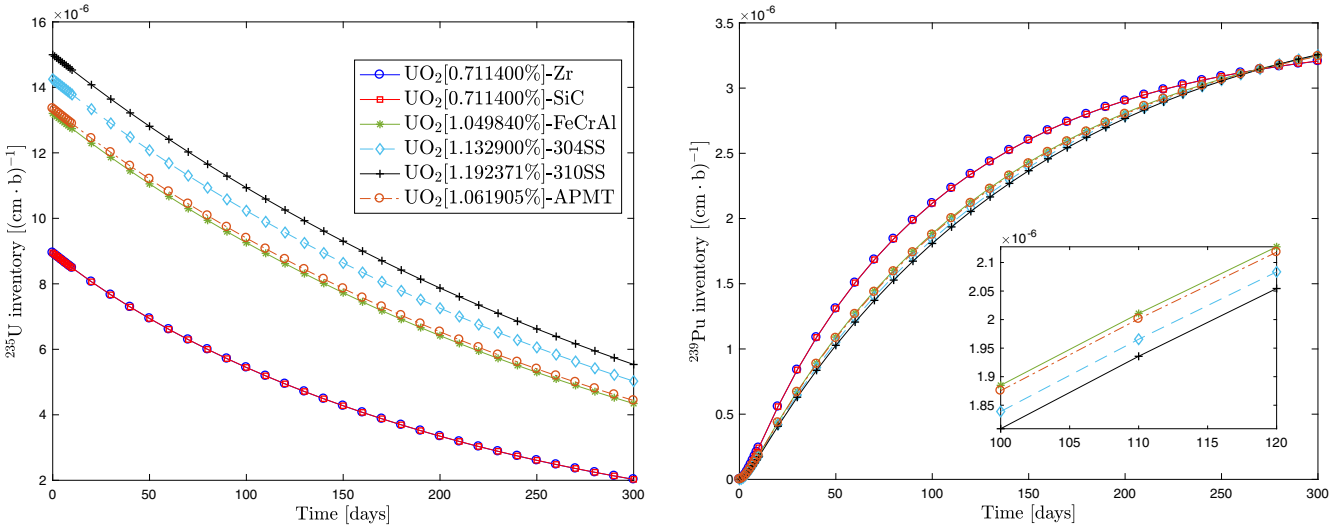

Fig. 6. ^{235}U (*left*) and ^{239}Pu (*right*) inventories during fuel depletion.

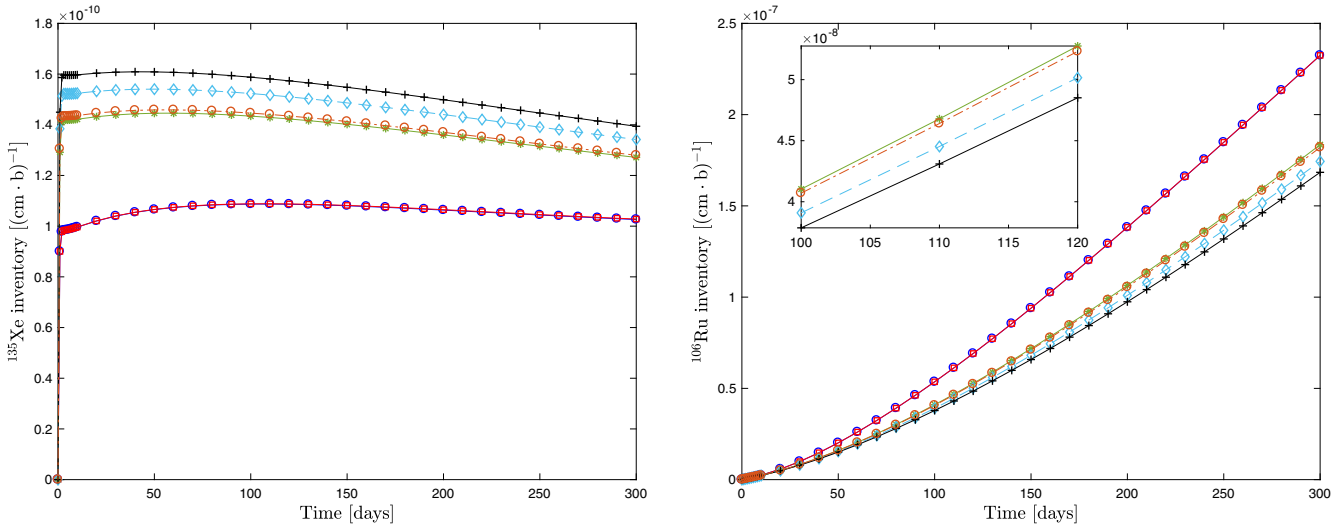

Fig. 7. ^{135}Xe (*left*) and ^{106}Ru (*right*) inventories during fuel depletion.

Table 6
Time average fuel absorption rate divided by cladding absorption rate for slow, epithermal and fast neutrons.

	Slow	Epithermal	Fast
UO_2/SiC	203.7	1457.7	271.8
UO_2/Zr	134.9	78.6	90.6
UO_2/FeCrAl	8.1	75.6	96.8
UO_2/APMT	8.0	35.4	81.3
UO_2/304SS	6.8	56.6	58.3
UO_2/310SS	6.2	49.6	40.8

for each time step. Fig. 8 compares the fuel regions homogenized lethargy flux spectra (normalized flux per unit lethargy) at the 150th day (middle of cycle or MOC). The two category behavior discussed before can only be differentiated in the thermal region. More neutron absorbing materials allow fewer thermal neutrons to reach the fuel. Therefore thermal peaks are staggered (lower for FeCrAl, APMT, 304SS and 310SS), while fast peaks are superimposed. The fast neutron fraction in enriched cells increases, which means a hardened neutron flux spectrum. This spectral hardening was found at every depletion step in fuel, cladding and moderator mixtures. For 0.0253 eV, ϕ_m^g peak is 30.5% higher in SiC and Zr fuel pins than in FeCrAl, APMT, 304SS and 310SS pins. Thus, the ^{239}Pu production rate is larger in Zr and SiC cells (as shown in Fig. 6, *right*). Consequently, in the case of spectral hardening, there is less accumulation of actinides and fission products (see ^{106}Ru inventory in Fig. 7, *right*) and a minimum of 50% more ^{135}Xe poison inventory (see Fig. 7, *left*). Despite a higher enrichment, the system reactivity

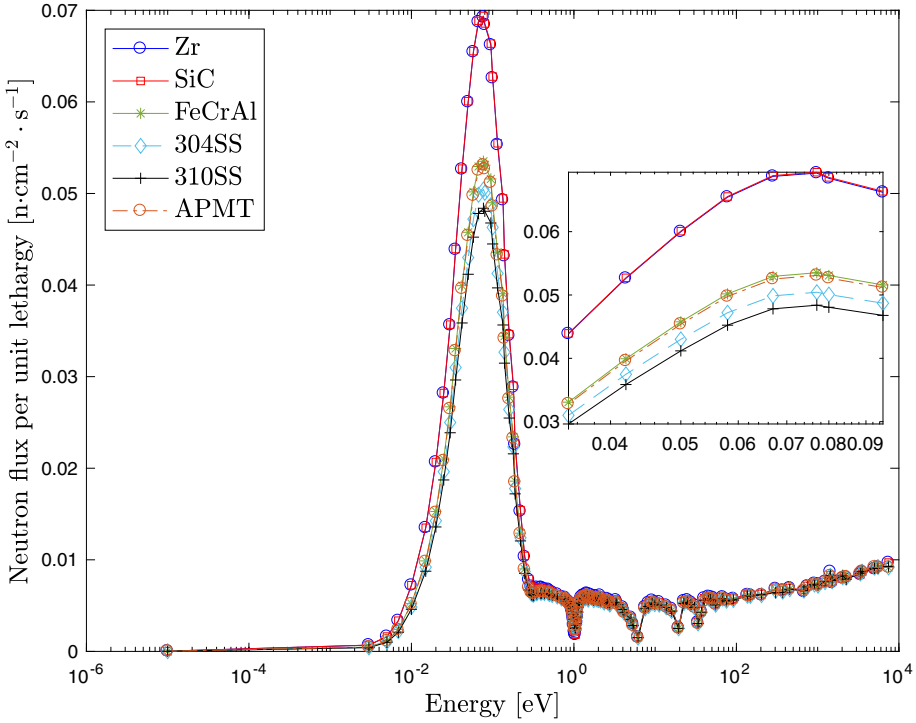

Fig. 8. Neutron flux spectrum at MOC.

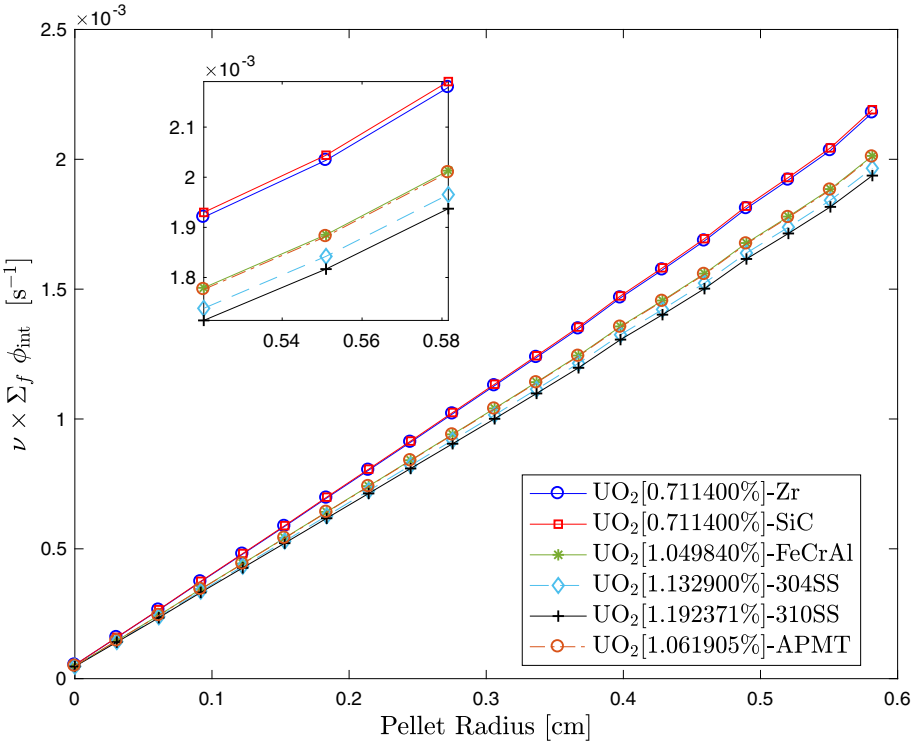

Fig. 9. Thermal fission neutron production rate radial profile at MOC.

is more quickly reduced. The same phenomenon was observed by George et al., 2015 for the PWR reactors, while introducing the same claddings, and by Chen and Yuan, 2017 for the LWR, while examining a new fuel cladding combination (U_3Si_2-FeCrAl).

3.3. Radial profile study

Fission rate spatial and temporal evolution and fissile plutonium production near the pellet periphery (the so-called "rim effect") could be affected when the cladding is changed (Piro et al., 2013). The fuel utilization factor will differ radially in the pellet. As a result, pin safety, performance and microstructure evolution could be affected. To analyze radial performance, each fuel pellet was divided into 20 equal area rings. Neutron flux was homogenized over pellets' subregions, cladding and coolant. Fission rates, power density and fissile isotopic production were computed at BOC, MOC and EOC (end of cycle) for fast, epithermal and slow range. Fig. 9 illustrates the fission neutron production rate ($\nu\Sigma_f\phi_{\rm int}$) by thermal neutrons as a function of the radial position in the pin at MOC, where $\phi_{\rm int}$ (cm/s) is the volume-integrated thermal flux. After moderation, thermal neutrons penetrate the bundle. By successfully passing through the sheath, they are largely captured in the fuel pin outer regions. Fissile nuclei in the interior regions are exposed to a much smaller fluence. Consequently, the fission rate is larger as we approach the pellet-sheath interface. All cladding materials show radially the same fission rate profile. Fission rate is 7.6% smaller in FeCrAl, APMT, 304SS and 310SS because of their spectral hardening. A steeper rise in the fission rates as a function of the radial position means a clad material with lower capture cross section.

The optimum use of both fissile and fertile materials is an important aspect in CANDU reactors. The breeding ratio (BR) describes the efficiency with which fuel is being utilized. When the number of fissile nuclei produced exceeds the number of fissile nuclei consumed, BR is superior to unity. A higher conversion ratio is required due to the fact that the reactor's decline in reactivity is slowed down by efficient captures in fertile nuclei as ^{235}U is consumed (Glasstone and Sesonske, 2012). Thermal and resonance neutron captures in ^{238}U produce ^{239}Pu. In order to study the plutonium spatial distribution, 20 identical fuel mixtures were defined for each pellet subring, where different burnup rates were allowed in every subregion. The ^{239}Pu radial profile inventory was then produced at every depletion step. Fig. 10 depicts the plutonium inventory as a function of fuel radius at MOC and EOC. Because of spatial self-shielding, ^{238}U capture reactions are more probable near the pellet periphery. Consequently, the ^{239}Pu concentration and BR ratios are greater in the outer regions. Comparing ^{239}Pu yield for different clad compositions, a certain gap was found between class I (Zr, SiC) and class II materials (FeCrAl, APMT, 304SS, 310SS).

At MOC, this gap is of the order of 7% in the pellet center, whereas it is reduced to 0.7% in the same region at EOC. Moreover, it varies from 7% up to 6.2% on the pellet periphery at MOC, while at EOC it decreases nearly exponentially as one moves towards the pin center. The difference can be explained by the spectrum hardening and enrichment effects. The ^{239}Pu inventory, for each time step and subregion, decreases as the cladding neutron capture cross section increases. Also, a higher ^{235}U nucleus presence at each time step implies higher fissile absorption probability than fertile capture chance. At the 280th day, ^{239}Pu concentration in the outer region becomes slightly higher for the cells cladded with FeCrAl, APMT, 304SS and 310SS. Throughout the fuel residence time, total plutonium concentration is lower in optimized cells. At EOC, over 60% more ^{235}U will be left in the optimized cell and a nearly identical plutonium concentration will be left in all cells (see Fig. 6). We conclude that a much higher fuel economy is observed in fuel pins cladded with SiC and Zr.

3.4. Geometry optimization

Natural uranium fueled cells cladded with class II materials remain subcritical during all depletion cycle, so a fuel enrichment was required to sustain the chain reaction at $\bar{k}_{\rm eff,Zr}$. After enrich-

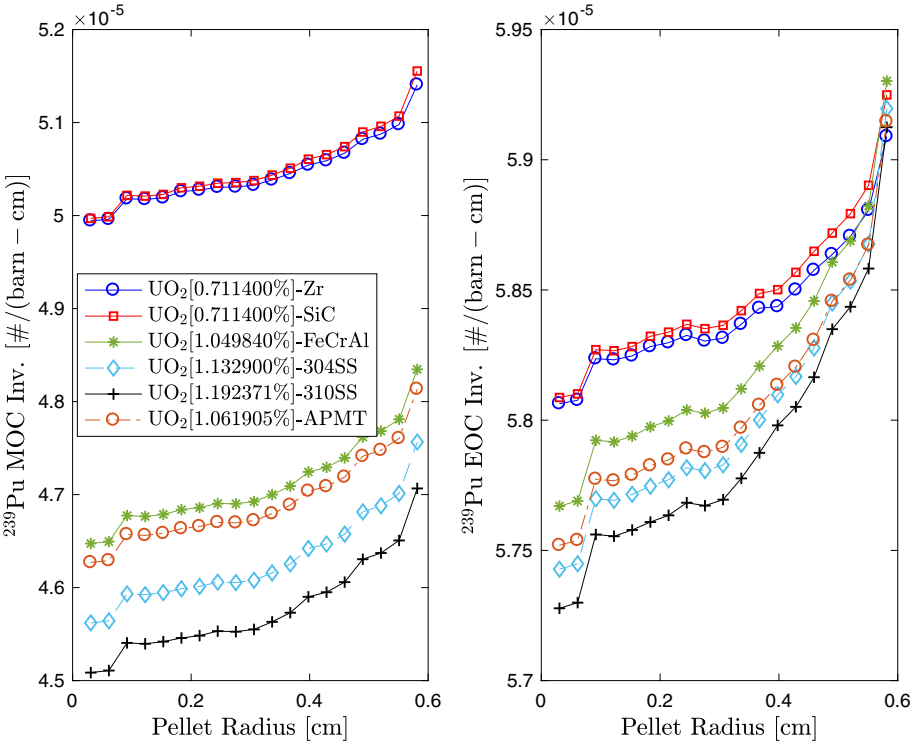

Fig. 10. ^{239}Pu radial profile at MOC (*left*) and EOC (*right*).

ment, some disadvantages persist like the spectral hardening, the lower fission rate and the lower conversion factor. Sheath thickness was reduced by 200 μm to compensate the cladding effect and mitigate the neutronic penalty. Fig. 11 presents k_{eff} as a function of the fuel residence time for the first geometry optimization case ($\mathcal{C}_1$ and $\mathcal{C}_4$). Depletion results for the second ($\mathcal{C}_2$ and $\mathcal{C}_5$) and the third ($\mathcal{C}_3$ and $\mathcal{C}_6$) pin arrangements differ only by ∼100 pcm compared with Fig. 11. Such differences cannot be visually ascertained and the figures have not been presented. For the reference case ($\mathcal{C}_0$: $e_{\text{enrU}}, \epsilon = 418$ μm), Table 7 summarizes the criticality level

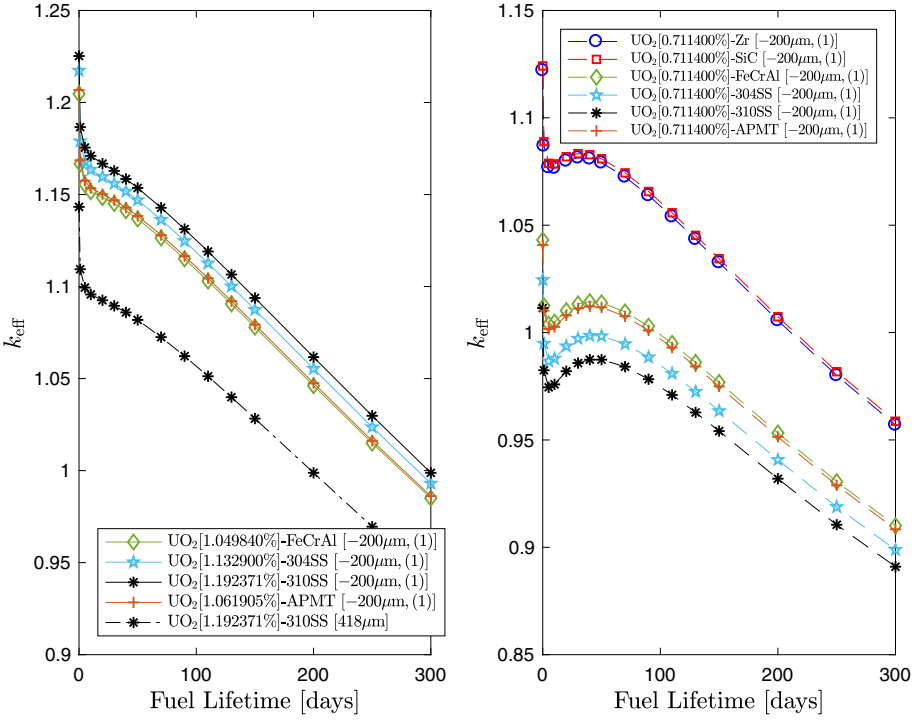

Fig. 11. Test (1). Variation of k_{eff} with time for cells with optimized enrichment [Cases $\mathcal{C}_0$ and $\mathcal{C}_1$ from Table 4] (*left*) and with natural enrichment [$\mathcal{C}_4$ from Table 4] (*right*).

Table 7
k_{eff} at BOC and time-averaged k_{eff} for Case ($\mathcal{C}_0$) fuel pin configuration (optimized enrichment and reference geometry configuration).

	Zr	SiC	FeCrAl	304SS	310SS	APMT
$k_{\text{eff}}(t_0, \mathcal{C}_0)$	1.118047	1.122149	1.141111	1.142709	1.143292	1.141600
$\bar{k}_{\text{eff}}(\mathcal{C}_0)$	1.026239	1.029790	1.026239	1.026239	1.026239	1.026239

at BOC and the time-averaged k_{eff}. For all configurations proposed (Case $\mathcal{C}_1$ to $\mathcal{C}_6$), Table 8 lists the cycle reactivity differences with respect to the reference case ($\mathcal{C}_0$).

Decreasing the cladding thickness by reducing the cladding outer radius ($\mathcal{C}_1$) results in a 66 mk gain in $\bar{k}_{\text{eff}}$ in the case of 310SS compared to only 1 mk for SiC. Using the same fuel rod configurations with e_{natU} ($\mathcal{C}_4$) allowed class II cells to start the depletion cycle supercritical (see Fig. 11, *right*). This conclusion remains valid for tests ($\mathcal{C}_5$) and ($\mathcal{C}_6$). Such a configuration requires less enrichment to reach $\bar{k}_{\text{eff,Zr}}$ and the spectrum effect should be less pronounced. Reducing the cladding thickness by increasing the pellet outer radius ($\mathcal{C}_2$) induces a more positive $\Delta\bar{k}_{\text{eff}}$ response. This phenomenon can be explained by a higher fissile material volume. The gain is higher for cells cladded with class II materials because there is more ^{235}U at BOC and during the entire cycle. Diminishing the cladding thickness by introducing a void gap ($\mathcal{C}_3$) gives the lowest $\bar{k}_{\text{eff}}$ improvements for all cells (larger clad volume than for $\mathcal{C}_1$ without the additional fuel of $\mathcal{C}_2$ to compensate for clad absorption). The opposite effect is observed when the vacuum gap and the cladding positions are interchanged (as in the hypothetical example $\mathcal{C}_3^h$) because of the additional reduction in the coolant volume with respect to $\mathcal{C}_1$.

We conclude that decreasing the cladding thickness leads to a more enhanced reactivity in iron and steel-based cells. Optimizing the cladding thickness by increasing the fuel volume ($\mathcal{C}_2$) induces the best improvements of $\bar{k}_{\text{eff}}$, followed by coolant volume increase ($\mathcal{C}_1$) and finally the void gap increase ($\mathcal{C}_3$). In other words, balance between neutronic capture and enrichment penalties could be more adapted by choosing one of Case 1–3 new configurations. From a safety standpoint, reducing the cladding thickness by more than 200 μm is not desirable and the capability of fission products retention, for such a thin clad, should be investigated.

3.5. Reactivity perturbations

During normal operations, the CANDU-6 reactor is continuously refueled by an appropriate rate of fuel replacement (Rouben, 1984). Cells based on FeCrAl, APMT, 304SS and 310SS cladding need enriched uranium fuel, which has a much larger excess reactivity than current CANDU fuel. A small reactivity perturbation in a critical state can make the reactor power diverge (Rozon, 1998; Lewins, 2013). It is not known yet how the cells would react for these candidate claddings to temperature and density perturbations. Here, we compare the six cell responses when the following perturbation scenarii on local parameters are examined:

1. the coolant temperature T_c is adjusted separately by $\pm$10 K, $\pm$20 K and $\pm$30 K.
2. the moderator temperature T_m is adjusted separately by $\pm$10 K, $\pm$20 K and $\pm$30 K.
3. the fuel temperature T_f is adjusted separately by $\pm$100 K, $\pm$200 K and $\pm$300 K.
4. the coolant density ρ_v^c is reduced by $-1\%, -5\%, -10\%, -50\%, -70\%$ and -100%.
5. the moderator density ρ_v^m is reduced by $-1\%, -5\%, -10\%$ and -50%.
6. both the coolant density and temperature (T_c, ρ_v^c) are simultaneously perturbed.
7. both the coolant density and the fuel temperature (T_f, ρ_v^c) are simultaneously perturbed.

The system criticality is computed by measuring its deviation from the Rayleigh reference ratio $\lambda = M\phi/F\phi$, where M represents the total neutron removal operator (losses by leakage and interactions) and F the total fission neutron production operator (prompt and delayed fissions). At each depletion step, the departure from $\lambda_{\text{ref}} = 1/k_{\text{eff,ref}}$ (optimized case $\mathcal{C}_0$ presented in Fig. 4) measures the cell criticality variation and defines its dynamic reactivity $\rho(t)$ (Rozon, 1998). When perturbations occur, we evaluate the perturbed effective multiplication factor $k_{\text{eff,per}}$ and compute:

$$\rho(t) = \left(\frac{1}{k_{\text{eff,ref}}(t)} - \frac{1}{k_{\text{eff,per}}(t)}\right) \times 1000 \text{ [mk]}. \quad (2)$$

Table 8
k_{eff} difference (initial and cycle average) with respect to the reference case ($\mathcal{C}_0$) for alternate fuel pin configurations ($\mathcal{C}_1$ to $\mathcal{C}_6$).

	Zr	SiC	FeCrAl	304SS	310SS	APMT
$\Delta k_{\text{eff}}(t_0, \mathcal{C}_1)$ [mk]	+3.99	+2.02	+63.54	+74.65	+81.95	+65.17
$\Delta\bar{k}_{\text{eff}}(\mathcal{C}_1)$ [mk]	+3.18	+1.47	+49.94	+59.53	+65.95	+51.42
$\Delta k_{\text{eff}}(t_0, \mathcal{C}_4)$ [mk]	+3.99	+2.02	−97.98	−118.18	−131.87	−100.87
$\Delta\bar{k}_{\text{eff}}(\mathcal{C}_4)$ [mk]	+3.18	+1.47	−53.90	−67.50	−77.09	−55.81
$\Delta k_{\text{eff}}(t_0, \mathcal{C}_2)$ [mk]	+3.50	+1.47	+64.45	+75.86	+83.37	+66.09
$\Delta\bar{k}_{\text{eff}}(\mathcal{C}_2)$ [mk]	+4.38	+2.63	+51.92	+61.65	+68.18	+53.39
$\Delta k_{\text{eff}}(t_0, \mathcal{C}_5)$ [mk]	+3.50	+1.47	−95.90	−115.54	−128.86	−98.74
$\Delta\bar{k}_{\text{eff}}(\mathcal{C}_5)$ [mk]	+4.38	+2.63	−50.60	−63.74	−73.01	−52.47
$\Delta k_{\text{eff}}(t_0, \mathcal{C}_3)$ [mk]	+5.68	+3.77	+62.99	+73.67	+80.70	+64.56
$\Delta\bar{k}_{\text{eff}}(\mathcal{C}_3)$ [mk]	+4.28	+2.62	+49.41	+58.67	+64.87	+50.84
$\Delta k_{\text{eff}}(t_0, \mathcal{C}_6)$ [mk]	+5.68	+3.77	−98.78	−119.47	−133.50	−101.74
$\Delta\bar{k}_{\text{eff}}(\mathcal{C}_6)$ [mk]	+4.28	+2.62	−54.71	−68.69	−78.54	−56.67
$\Delta k_{\text{eff}}(t_0, \mathcal{C}_3^h)$ [mk]	+6.39	+4.23	+71.59	+83.82	+91.87	+73.39
$\Delta\bar{k}_{\text{eff}}(\mathcal{C}_3^h)$ [mk]	+4.81	+2.94	+56.17	+66.76	+73.87	+57.80
$\Delta k_{\text{eff}}(t_0, \mathcal{C}_6^h)$ [mk]	+6.39	+4.23	−89.58	−108.50	−121.33	−92.30
$\Delta\bar{k}_{\text{eff}}(\mathcal{C}_6^h)$ [mk]	+4.81	+2.94	−47.99	−60.65	−69.61	−49.75

Table 9
Reactivity ρ [mk] at BOC following perturbations in coolant (ΔT_c), moderator (ΔT_m) and fuel (ΔT_f) temperature.

ΔT_c	Zr	SiC	FeCrAl	304SS	310SS	APMT
−30 K	+0.36	+0.36	+0.24	+0.22	+0.21	+0.24
−20 K	+0.24	+0.24	+0.16	+0.15	+0.14	+0.16
−10 K	+0.12	+0.12	+0.08	+0.07	+0.07	+0.08
+10 K	−0.12	−0.12	−0.08	−0.07	−0.07	−0.08
+20 K	−0.24	−0.24	−0.16	−0.15	−0.14	−0.16
+30 K	−0.36	−0.36	−0.24	−0.22	−0.21	−0.24
ΔT_m	Zr	SiC	FeCrAl	304SS	310SS	APMT
−30 K	+0.72	+0.71	+0.62	+0.60	+0.59	+0.62
−20 K	+0.49	+0.48	+0.42	+0.41	+0.40	+0.42
−10 K	+0.25	+0.24	+0.21	+0.21	+0.20	+0.21
+10 K	−0.25	−0.24	−0.21	−0.21	−0.20	−0.21
+20 K	−0.49	−0.48	−0.42	−0.41	−0.40	−0.42
+30 K	−0.73	−0.72	−0.64	−0.62	−0.61	−0.63
ΔT_f	Zr	SiC	FeCrAl	304SS	310SS	APMT
−300 K	+3.90	+3.91	+3.62	+3.58	+3.55	+3.60
−200 K	+2.53	+2.54	+2.35	+2.32	+2.31	+2.33
−100 K	+1.23	+1.23	+1.14	+1.13	+1.12	+1.13
+100 K	−1.16	−1.16	−1.08	−1.07	−1.06	−1.07
+200 K	−2.28	−2.29	−2.12	−2.09	−2.08	−2.10
+300 K	−3.37	−3.38	−3.12	−3.09	−3.06	−3.10

Tables 9 and 10 present the cell reactivity responses at BOC while Tables 11 and 12 list the same responses at MOC. Fig. 12 depicts the dynamic reactivity evolution for selected perturbations. All data presented was derived by evolving the bundle under reference conditions and applying the perturbations separately at each burnup step.

3.5.1. Coolant temperature perturbations

For both class I and II materials, increasing the coolant temperature, at BOC, produces negative variations in the system criticality (Table 9, *part I*). In the coolant, fission neutrons are in thermal equilibrium with heavy water isotopes. Assuming a Maxwell–Boltzmann distribution, the most probable neutron energy is $(3k_BT_c/2)$, where k_B is the Boltzmann constant. The neutron mean velocity is then $v = \sqrt{3k_BT_c/m}$. Consequently, if the coolant temperature increases, the neutrons are faster. The average energy of the slowed down neutrons slightly increases which results in a lower rate of fission in ^{235}U, the only fissile isotope in CANDU fresh bundles. Increasing the coolant temperature at MOC (Table 11, *part I*) results in an opposite effect to that observed at BOC, because of the contribution of ^{239}Pu resonance (0.3 eV). Reactivity increases with burnup (Fig. 12) because more and more ^{239}Pu is accumulated as the fuel depletes. The higher reactivity values were found in Zr and SiC bundles, followed by both FeCrAl and APMT, 304SS and finally 310SS. This order complies with plutonium evolution inventory in Fig. 6, plutonium radial profile in Fig. 10 and the increasing capture cross section of the claddings in the thermal-epithermal region (Fig. 2).

3.5.2. Moderator temperature perturbations

Table 9, *part II*, shows that increasing the moderator temperature has exactly the same global effect as for the coolant. The phenomenon is the same as that previously explained (thermal equilibrium and faster neutron returns). The difference is that, at

Table 10
Reactivity ρ [mk] at BOC following volumetric mass density perturbations $\Delta\rho_v^c$ in coolant, $\Delta\rho_v^m$ in moderator, simultaneous perturbations $(\Delta T_c, \Delta\rho_v^c)$ in coolant and $(\Delta T_f, \Delta\rho_v^c)$ in both fuel and coolant.

$\Delta\rho_v^c$	Zr	SiC	FeCrAl	304SS	310SS	APMT
−2.5%	+0.37	+0.37	+0.34	+0.34	+0.33	+0.34
−5%	+0.75	+0.74	+0.68	+0.67	+0.67	+0.68
−10%	+1.51	+1.48	+1.36	+1.34	+1.33	+1.36
−50%	+7.64	+7.51	+6.88	+6.76	+6.70	+6.87
−70%	+10.79	+10.60	+9.70	+9.51	+9.43	+9.68
−100%	+15.67	+15.39	+14.04	+13.74	+13.61	+14.01
$\Delta\rho_v^m$	Zr	SiC	FeCrAl	304SS	310SS	APMT
−1%	−1.65	−1.63	−1.64	−1.65	−1.65	−1.67
−5%	−3.44	−3.40	−3.42	−3.43	−3.44	−3.47
−10%	−7.48	−7.39	−7.42	−7.45	−7.47	−7.53
−50%	−80.23	−79.22	−78.49	−78.63	−78.68	−79.59
$(\Delta T_c, \Delta\rho_v^c)$	Zr	SiC	FeCrAl	304SS	310SS	APMT
(+30 K,−8.79%)	+0.99	+0.97	+0.98	+0.98	+0.98	+0.98
(+20 K,−5.55%)	+0.61	+0.60	+0.61	+0.60	+0.61	+0.61
(+10 K,−2.68%)	+0.29	+0.28	+0.29	+0.29	+0.29	+0.29
(−10 K,+2.57%)	−0.26	−0.26	−0.27	−0.27	−0.27	−0.27
(−20 K,+4.93%)	−0.49	−0.48	−0.50	−0.51	−0.51	−0.51
(−30 K,+7.16%)	−0.69	−0.67	−0.72	−0.72	−0.73	−0.72
$(\Delta T_f, \Delta\rho_v^c)$	Zr	SiC	FeCrAl	304SS	310SS	APMT
(+300 K,−100%)	+12.46	+12.17	+11.10	+10.84	+10.73	+11.09

Table 11
Reactivity ρ [mk] at MOC following perturbations in coolant (ΔT_c), moderator (ΔT_m) and fuel (ΔT_f) temperature.

ΔT_c	Zr	SiC	FeCrAl	304SS	310SS	APMT
−30 K	−0.64	−0.63	−0.42	−0.37	−0.35	−0.46
−20 K	−0.43	−0.42	−0.28	−0.25	−0.23	−0.32
−10 K	−0.21	−0.21	−0.14	−0.13	−0.12	−0.18
+10 K	+0.22	+0.21	+0.14	+0.13	+0.12	+0.09
+20 K	+0.45	+0.44	+0.29	+0.26	+0.24	+0.24
+30 K	+0.68	+0.67	+0.45	+0.40	+0.38	+0.39
ΔT_m	Zr	SiC	FeCrAl	304SS	310SS	APMT
−30 K	−2.67	−2.64	−1.85	−1.70	−1.60	−1.87
−20 K	−1.84	−1.82	−1.29	−1.18	−1.11	−1.31
−10 K	−0.93	−0.91	−0.65	−0.60	−0.56	−0.69
+10 K	+0.94	+0.92	+0.66	+0.61	+0.57	+0.60
+20 K	+1.89	+1.86	+1.34	+1.23	+1.16	+1.27
+30 K	+2.87	+2.83	+2.04	+1.89	+1.78	+1.96
ΔT_f	Zr	SiC	FeCrAl	304SS	310SS	APMT
−300 K	+0.60	+0.66	+1.64	+1.81	+1.93	+1.60
−200 K	+0.30	+0.34	+0.99	+1.12	+1.20	+0.96
−100 K	+0.09	+0.11	+0.44	+0.51	+0.55	+0.40
+100 K	+0.02	+0.00	−0.34	−0.41	−0.44	−0.40
+200 K	+0.09	+0.05	−0.63	−0.81	−0.84	−0.69
+300 K	+0.23	+0.16	−0.85	−1.07	−1.19	−0.90

Table 12
Reactivity ρ [mk] at MOC following volumetric mass density perturbations $\Delta\rho_v^c$ in coolant, $\Delta\rho_v^m$ in moderator, simultaneous perturbations $(\Delta T_c, \Delta\rho_v^c)$ in coolant and $(\Delta T_f, \Delta\rho_v^c)$ in both fuel and coolant.

$\Delta\rho_v^c$	Zr	SiC	FeCrAl	304SS	310SS	APMT
−2.5%	+0.32	+0.32	+0.34	+0.34	+0.34	+0.29
−5%	+0.64	+0.64	+0.67	+0.67	+0.68	+0.63
−10%	+1.29	+1.27	+1.34	+1.35	+1.36	+1.30
−50%	+6.50	+6.39	+6.76	+6.78	+6.82	+6.74
−70%	+9.17	+9.00	+9.52	+9.55	+9.60	+9.51
−100%	+13.31	+13.06	+13.80	+13.81	+13.89	+13.80
$\Delta\rho_v^m$	Zr	SiC	FeCrAl	304SS	310SS	APMT
−1%	−1.95	−1.94	−1.91	−1.90	−1.90	−1.98
−5%	−4.07	−4.04	−3.97	−3.96	−3.96	−4.07
−10%	−8.83	−8.76	−8.61	−8.60	−8.59	−8.77
−50%	−93.77	−92.81	−90.80	−90.57	−90.37	−92.00
$(\Delta T_c, \Delta\rho_v^c)$	Zr	SiC	FeCrAl	304SS	310SS	APMT
(+30 K,−8.79%)	+1.76	+1.73	+1.59	+1.56	+1.54	+1.54
(+20 K,−5.55%)	+1.14	+1.12	−0.95	+1.00	+0.99	−1.00
(+10 K,−2.68%)	+0.56	+0.55	−0.49	+0.49	+0.48	−0.54
(−10 K,+2.57%)	−0.55	−0.54	+0.50	−0.47	−0.47	+0.45
(−20 K,+4.93%)	−1.08	−1.06	+1.02	−0.93	−0.91	+0.97
(−30 K,+7.16%)	−1.61	−1.58	+1.59	−1.37	−1.34	+1.54
$(\Delta T_f, \Delta\rho_v^c)$	Zr	SiC	FeCrAl	304SS	310SS	APMT
(+300 K,−100%)	+13.89	+13.56	+13.23	+13.04	+12.95	+13.22

MOC, reactivity values are ∼ 4 times more pronounced than for T_c perturbations. This is because the moderator volume is 83% of the CANDU reactor core, which can be compared with 4% for the coolant (Griffiths, 1983; Whitlock, 1995).

3.5.3. Fuel temperature perturbations

Table 9, *part III*, shows that all bundles' reactivity decreases as the fuel temperature increases. This behavior is mainly due to the Doppler effect: as ΔT_f is increased, resonance broadening increases the neutron radiative capture for ^{238}U. At MOC (Table 11, *part III*), assuming a positive perturbation $\Delta T_f = +100, +200$ and +300 K, a positive reactivity is observed for SiC and Zr bundles. This effect is caused by ^{239}Pu contributions. Reactivity values are two times higher at BOC because all bundles were freshly fueled. Fig. 12 shows that the Doppler effect remains higher for Zr and SiC bundles, until the 5th day, because less ^{238}U captures occur in enriched cells. Table 9, *part III*, and Table 5 show that, at BOC, the higher Doppler coefficient correspond to the rank of the lower enrichment needed. After that period, the behaviors are completely inverted because a higher ^{239}Pu fission rate is observed in the natural cells.

3.5.4. Coolant density perturbations

Coolant partial voiding can be caused by a fuel overpower, excessive heat flux and then a coolant boiling. Coolant complete evaporation can be caused by a loss of power to the circulating pumps. In pressure-tube thermal reactors (CANDU and RBMK), such effects are confined to the coolant and the moderator is not directly affected (Rozon, 1998). As one can see, a complete loss in cooling capacity makes the system prompt supercritical. Tables 10 and 12, *parts I*, show that for all cells, the reactivity increases as the coolant voiding percentage increases.

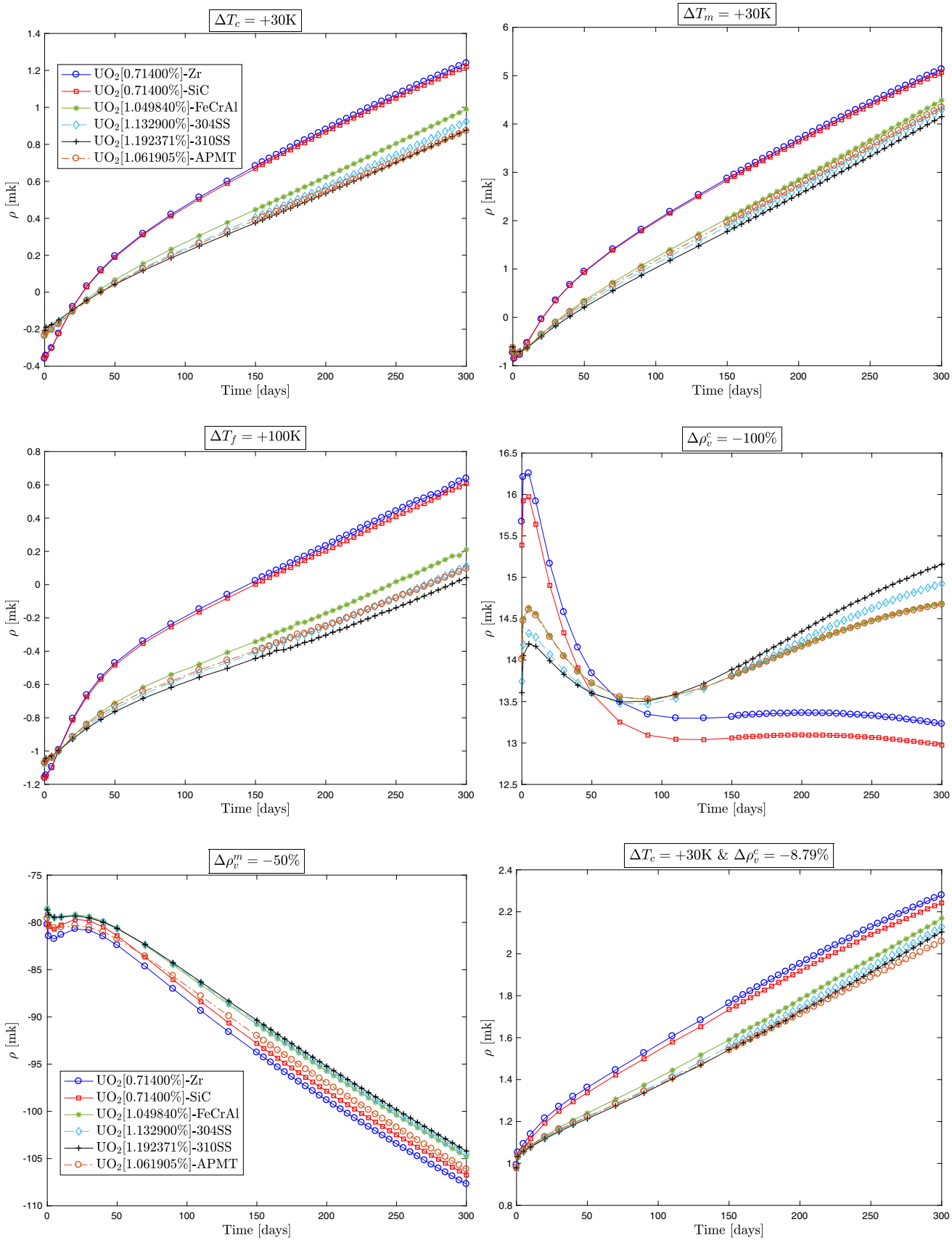

Fig. 12. Various perturbations scenarios illustrated.

In CANDU reactors, the coolant occupies 4% of the cell volume. Its moderation role can be neglected in comparison with the moderator contribution. Fuels rods are the main sources of fast neutrons (0.821 MeV up to 10 MeV) while the moderator is the major source of the thermal neutrons ($\leqslant 0.625$ eV). One role of the coolant is to slow down fast neutron to epithermal energies. Removing the coolant role increase reactivity by decreasing resonance absorption in the pin rods (resonance escape probability p increases). In addition, the coolant only contributes 0.03% of all the absorptions in the cell (Whitlock, 1995). Thus, decreasing the coolant density will not affect the overall absorption. Fast fission rates also increase since less scattering takes place and the fast neutrons can reach a neighboring fuel pin. Whitlock et al., 1995 showed that at zero burnup "31% of the total effect is due to the thermal factors ($\eta + f$), 7% is due to the fast factors (p_f and ϵ) and 62% is due to the epithermal factor (p_e)". When the ^{239}Pu concentration in the fuel increases, a change occurs in the reproduction factor η and a reduction in f component (neutron spectrum is shifted away from ^{239}Pu and ^{241}Pu significant thermal fission resonance), which imply a net negative effect. Thus, this contribution to the void effect is zero at BOC (fresh fuel) and slightly negative at MOC (equilibrium fuel). Consequently, bundles containing higher ^{239}Pu concentration (Zr and SiC) see a larger decrease of their coolant void reactivity with burnup (Table 12, *part I*).

3.5.5. Moderator density perturbations

Tables 10–12, *parts II*, show that the cells reactivity decreases as the moderator voiding rate increases. This result is opposite to the behavior observed for the coolant. The flux reaching the moderator is an epithermal flux. When the moderator density decreases, the thermalization process is less efficient. Neutrons that return are more energetic than in normal operation conditions. Neutrons pass far from ^{235}U and ^{239}Pu resonances, which explains the negative voiding coefficient. Moderator voiding effect is slightly more negative in Zr and SiC bundles.

3.5.6. Simultaneous perturbations in coolant temperature and density

The reactivity of all cells increase as we both decrease the coolant density and increase the coolant temperature. D_2O density was computed according to the assumed ΔT_c perturbation and the coolant purity, using WIMS-AECL temperature tabulations (Marleau et al., 2016). The simultaneous effect ($+30$K, -9%), at MOC, for FeCrAl (for example) produced a reactivity of $+1.6$mk, which is, approximately, the sum of $+1.3$mk (perturbation $\Delta\rho_v^c = -10\%$, Table 12-*part I*) and $+0.4$ mk (perturbation $\Delta T_c = +30$ K, Table 11-*part I*). The overall effect is the sum of the individual effects, coolant density reduction being the slightly dominant effect. The overall effect is more pronounced in class I cells.

3.5.7. Simultaneous perturbations in coolant density and fuel temperature

Combining a complete loss of the coolant with an increase of $+300$ K in the fuel temperature increases the reactivity of all cells by a minimum of $+10.73$ mk (Table 10 and Table 12, *parts IV*). This perturbation is close to RIA conditions and allows another consideration of joint effects. Reactivity values are higher at MOC because more ^{239}Pu and ^{241}Pu fissions occur as fresh bundles deplete. As seen in Section 3.5.6, the overall effect is the sum of the individual effects. Table 10, *part IV*, shows that SiC reactivity increases by $+12.17$ mk, at BOC, which is approximately the sum of $+15.39$ mk (perturbation $\Delta\rho_v^c = -100\%$, Table 10-*part I*) and -3.38 mk (perturbation $\Delta T_f = +300$ K, Table 9-*part III*). For both BOC and MOC, reactivity increases are lower in ferritic and steel-cladded bundles.

4. Conclusion

The neutron economy performance for each cladding material is quantified in comparison with the baseline zirconium alloy used in actual CANDU-6 reactors. UO_2 fuel bundle calculations are performed for iron-based alloys (FeCrAl and APMT), steel-based alloys (304SS and 310SS), silicon carbide (SiC) and Zircaloy (Zr-II) cladding. Ni-59 and Fe-56 high thermal captures imply a major neutron penalty for steel and iron-based claddings. The first serious consequence, for these alloys, is that a chain reaction can not be sustained in CANDU-6 actual conditions (fuel pin geometry and natural enrichment). The more neutron transparent SiC cladding results in the best neutron economy throughout the life cycle. A positive 0.35% Δk_{eff} from Zircaloy-II is produced in [UO_2, SiC] cell in the same CANDU-6 conditions. For iron and steel alloys, an enrichment methodology is developed to reach the CANDU-6 cell cycle averaged multiplication factor.

Increasing the enrichment causes the ^{239}Pu peak, observed in k_{eff} patterns, to disappear and induces a higher k_{eff} decreasing rate with burnup. The slow neutron absorption rate is found to be 203 times more pronounced in UO_2 pellet than in SiC cladding, while this ratio is reduced to 8 and 6, respectively, in iron and steel-based claddings. Spectral analysis is performed at every burnup steps for fuel, cladding and moderator. A spectral hardening is found in cells made with FeCrAl, APMT, 304SS and 310SS, that induces a lower accumulation of actinides and fission products. Neutron flux spectrum (ϕ_m^g) is found 30.5% higher at 0.0253 eV in SiC and Zr cells, leading to lower ^{239}Pu production in enriched cells. A minimum of 50% more xenon poison is produced at end-of-cycle in iron and steel-based bundles. All cells showed radially a similar fission rate and plutonium inventory profiles. At MOC, on the pellet periphery, the fission rate and the plutonium concentration are found, respectively, 7.6% and 6.2% smaller in steel and iron-based alloys. At EOC, a minimum of 60% more fissile ^{235}U is left in the enriched cell. Three fuel pin configurations are examined in both natural ($e_{\text{nat U}}$) and optimized ($e_{\text{enr U}}$) enrichment conditions to compensate the cladding effect. Reducing the sheath thickness by 200 μm allowed iron and steel-based cells to start the depletion cycle supercritical in $e_{\text{nat U}}$ condition. Decreasing the cladding thickness always has a larger impact for iron and steel-based cells. By perturbing coolant and moderator densities and temperatures, and fuel temperature, different moderate and severe DB scenarios are simulated at BOC and MOC. Burnup calculations are performed under nominal conditions. At zero burnup, fuel temperature coefficients (Doppler effect) are higher in SiC and Zr bundles. After plutonium accumulation (MOC), this behavior is inverted. At mid-burnup, the coolant voiding effect is slightly higher in bundles made with iron and steel-based alloys while at BOC it was lower.

Based on these results, future work will consider the second level of our computational scheme, namely full-core calculations. We will then determine neutron poison requirements and analyze the reactor global behavior during normal and accidental operations scenarii. LOCA and RIA accidents will be simulated and the new margins earned from Zircaloy-II case will be quantified.

Acknowledgments

The authors acknowledge the Natural Sciences and Engineering Research Council of Canada (NSERC) for partly funding this work. The authors thank Yasamin Majedi for her valuable help in grammar and speller checking.

References

Burns, P.C., Ewing, R.C., Navrotsky, A., et al., 2012. Nuclear fuel in a reactor accident. Sci. (Washington) 335 (6073), 1184–1188.

Chen, S., Yuan, C., 2017. Neutronic analysis on potential accident tolerant fuel-cladding combination U3Si2-FeCrAl. Science and Technology of Nuclear Installations 2017.

Cottingham, W., Greenwood, D., 2002. Introduction to Nuclear Physics. Taylor & Francis.

George, N.M., Terrani, K., Powers, J., Worrall, A., Maldonado, I., 2015. Neutronic analysis of candidate accident-tolerant cladding concepts in pressurized water reactors. Ann. Nucl. Energy 75, 703–712. URL:http://www.sciencedirect.com/science/article/pii/S0306454914004770.

Glasstone, S., Sesonske, A., 2012. Nuclear Reactor Engineering: Reactor Systems Engineering. Springer Science & Business Media.

Griffiths, J., 1983. Reactor Physics and Economic Aspects of the CANDU Reactor System. Chalk River Nuclear Laboratories, Chalk River, Ont..

Hébert, A., Marleau, G., 1991. Generalization of the Stammler method for the self-shielding of resonant isotopes in arbitrary geometries. Nucl. Sci. Eng. 108 (3), 230–239.

Koning, A., Forrest, R., Kellett, M., Mills, R., Henriksson, H., Rugama, Y., et al., 2006. The JEFF-3.1 nuclear data library. OECD.

Leppänen, J., 2013. Serpent–a continuous-energy Monte Carlo reactor physics burnup calculation code. VTT Technical Research Centre of Finland.

Lewins, J., 2013. Nuclear Reactor Kinetics and Control. Elsevier.

Marleau, G., 2005. New Geometries Processing in DRAGON: The NXT: Module. Institut de génie nucléaire, Département de génie physique, École Polytechnique de Montréal.

Marleau, G., Hébert, A., Roy, R., 1992. New computational methods used in the lattice code dragon. In: Topical Meeting on Advances in Reactor Physics, vol. 1, March 8–11, Charleston, SC.

Marleau, G., Hébert, A., Roy, R., 2016. A User Guide for DRAGON Version 5. Institut de génie nucléaire, Département de génie physique, École Polytechnique de Montréal.

Ott, L., Robb, K., Wang, D., 2014. Preliminary assessment of accident-tolerant fuels on LWR performance during normal operation and under DB and BDB accident conditions. J. Nucl. Mater. 448 (1–3), 520–533. URL:http://www.sciencedirect.com/science/article/pii/S002231151301129X.

Pint, B., Terrani, K., Brady, M., Cheng, T., Keiser, J., 2013. High temperature oxidation of fuel cladding candidate materials in steam hydrogen environments. J. Nucl. Mater. 440 (1–3), 420–427. URL:http://www.sciencedirect.com/science/article/pii/S0022311513007927.

Piro, M., Banfield, J., Clarno, K., Simunovic, S., Besmann, T., Lewis, B., Thompson, W., 2013. Coupled thermochemical, isotopic evolution and heat transfer simulations in highly irradiated UO2 nuclear fuel. J. Nucl. Mater. 441 (1), 240–251. URL: http://www.sciencedirect.com/science/article/pii/S0022311513008064.

Rouben, B., 1984. Le CANDU: étude du coeur et gestion du combustible. L'Énergie Atomique du Canada, Limitée, CANDU Operations, Mississauga, Ont..

Rouben, B., 2002. RFSP-IST, the industry standard tool computer program for CANDU reactor core design and analysis. In: The 13th Pacific Basin Nuclear Conference, October 21–25, 2002. Shenzhen, China.

Rouben, B., 2003. CANDU Fuel Management. Presentation at McMaster University.

Rozon, D., 1998. Introduction to Nuclear Reactor Kinetics. Polytechnic International Press.

St-Aubin, E., Marleau, G., 2015. Candu-6 fuel optimization for advanced cycles. Nucl. Eng. Des. 293 (Supplement C), 371–384. URL:http://www.sciencedirect.com/science/article/pii/S0029549315003301.

Terrani, K.A., Snead, L.L., Gehin, J.C., 2012. Microencapsulated fuel technology for commercial light water and advanced reactor application. J. Nucl. Mater. 427 (1–3), 209–224. URL:http://www.sciencedirect.com/science/article/pii/S0022311512002528.

Terrani, K.A., Zinkle, S.J., Snead, L.L., 2014. Advanced oxidation-resistant iron-based alloys for LWR fuel cladding. J. Nucl. Mater. 448 (1), 420–435.

Uwaba, T., Ito, M., Maeda, K., 2011. Diametral strain of fast reactor MOX fuel pins with austenitic stainless steel cladding irradiated to high burnup. J. Nucl. Mater. 416 (3), 350–357.

Varin, E., Roy, R., Baril, R., Hotte, G., 2004. CANDU-6 operation post-simulations using the reactor physics codes DRAGON/DONJON. Ann. Nucl. Energy 31 (18), 2139–2155.

Whitlock, J., Garland, W.J., Milgram, M., 1995. Effects contributing to positive coolant void reactivity in CANDU. Trans. Am. Nucl. Soc 72, 329.

Whitlock, J.J., 1995. Reduction of the Coolant Void Reactivity Effect in a CANDU Lattice Cell. McMaster University (Ph.D. thesis).

Zinkle, S.J., Terrani, K.A., Gehin, J.C., Ott, L.J., Snead, L.L., 2014. Accident tolerant fuels for LWRs: a perspective. J. Nucl. Mater. 448 (1), 374–379.